Plasma Physics and
Controlled Fusion

PURPOSE-LED
PUBLISHING™

ACCEPTED MANUSCRIPT • OPEN ACCESS

Full-discharge simulations of the TCV tokamak using the Fenix flight simulator

To cite this article before publication: Reinart Coosemans *et al* 2026 *Plasma Phys. Control. Fusion* in press https://doi.org/10.1088/1361-6587/ae6944

Manuscript version: Accepted Manuscript

Accepted Manuscript is "the version of the article accepted for publication including all changes made as a result of the peer review process, and which may also include the addition to the article by IOP Publishing of a header, an article ID, a cover sheet and/or an 'Accepted Manuscript' watermark, but excluding any other editing, typesetting or other changes made by IOP Publishing and/or its licensors"

This Accepted Manuscript is **© 2026 The Author(s). Published by IOP Publishing Ltd**.

As the Version of Record of this article is going to be / has been published on a gold open access basis under a CC BY 4.0 licence, this Accepted Manuscript is available for reuse under a CC BY 4.0 licence immediately.

Everyone is permitted to use all or part of the original content in this article, provided that they adhere to all the terms of the licence https://creativecommons.org/licences/by/4.0

Although reasonable endeavours have been taken to obtain all necessary permissions from third parties to include their copyrighted content within this article, their full citation and copyright line may not be present in this Accepted Manuscript version. Before using any content from this article, please refer to the Version of Record on IOPscience once published for full citation and copyright details, as permissions may be required. All third party content is fully copyright protected and is not published on a gold open access basis under a CC BY licence, unless that is specifically stated in the figure caption in the Version of Record.

View the article online for updates and enhancements.

This content was downloaded from IP address 94.31.72.233 on 22/05/2026 at 05:55

Full-discharge simulations of the TCV tokamak using the Fenix flight simulator

R. Coosemans[1], E. Fable[2], O. Sauter[1], P. David[2], F. Felici[1,3], C. Galperti[1], C. Heiß[1], A. Mele[1], A. Merle[1], A. Tenaglia[1,4], C. Wu[5], and the TCV Team‡

[1]Swiss Plasma Center, Ecole Polytechnique Fédérale de Lausanne, Lausanne, Switzerland
[2]Max-Planck-Institut für Plasmaphysik, 85748 Garching, Germany
[3]Google Deepmind, London, UK
[4]DICII, Università degli Studi di Roma "Tor Vergata", Roma, Italy
[5]Karlsruher Institut für Technologie, 76344 Eggenstein-Leopoldshafen, Germany

E-mail: reinart.coosemans@epfl.ch

February 2026

Abstract. The goal of this work is to develop a simulator for the TCV tokamak that self-consistently includes transport and equilibrium while taking the plant control systems into account. To achieve this, we adapted the Fenix flight simulator that was originally developed for ASDEX Upgrade for use on TCV. The MEQ-FGE free boundary equilibrium code that is widely used for TCV analysis as well as the TCV magnetic controller were coupled to this framework. In addition, a reduced transport model drawing inspiration from earlier RAPTOR modelling for TCV was implemented. Applying this simulator to discharges in the TCV database shows a good agreement of both kinetic and magnetic results with experimental measurements. In particular, it is illustrated how the shape controller is expected to stabilise discharges and it is found that details of the kinetic profiles can be important for the shape and the stability of the equilibrium. This work paves the way to using Fenix for discharge preparation and validation as well as controller development and validation for TCV.

Keywords: flight simulator, transport modelling, free boundary equilibrium, magnetic control

‡ See the author list of B. Duval et al, 2024 Nucl. Fusion 64, 112023

Accepted Manuscript

1. Introduction

As the next generation of high-power tokamaks is under construction, preparing safe operation of these machines becomes critical. Simulators of the tokamak plant that take into account its control system are vital tools to develop and validate both operational scenarios and controllers. As such, it is important to develop "flight simulators" and to validate them on existing machines. Employing such simulators on current machines will furthermore allow operators to build up experience using them, to gauge their accuracy, and to develop procedures for how and when to use them. In addition, having such tools available will already improve the efficiency of the operation of these existing tokamaks. In this context, this work has adapted the Fenix flight simulator [1, 2, 3] that has originally been developed for the ASDEX Upgrade tokamak for use on the TCV tokamak.

Next to Fenix, several other frameworks exist that couple transport simulations with free boundary magnetic equilibrium solvers and/or control algorithms for discharge design and scenario validation. The NEST (Nice Environement for Simulated Tokamak) flight simulator has recently been developed around the NICE equilibrium code [4] for the WEST tokamak [5]. A similar framework which additionally used the METIS code [6] for transport has also been used to simulate the JT60-SA tokamak [7]. These tools are likewise foreseen to be used at ITER. At the DIII-D tokamak, the FUSE framework is under development, which also aims to have the capability to simulate all these dynamics, next to even more extensive applications such as powerplant design and cost estimation [8]. Another framework combining transport, equilibrium, and control is the NSFsim code [9]. This package, notably aimed to be highly compatible with machine learning techniques, is based on the DINA code that includes both equilibrium and transport [10]. Also the COTSIM simulator, which is highly focused on optimising the profile kinetics of discharges and on the development of controllers for it, has been coupled to a free boundary equilibrium code recently [11].

For the TCV tokamak, mainly the MEQ suite of codes is used for equilibrium calculation [12]. The LIUQE equilibrium reconstruction code of this suite [13] has been coupled to the ASTRA [12, 14] and recently also to RAPTOR [15] transport codes for kinetic equilibrium reconstruction (KER). Furthermore, the inverse equilibrium solver FBT [13] has been coupled to RAPTOR to achieve the capability to take kinetic effects into account in equilibrium preparation [16]. Finally, the evolutive free boundary equilibrium variant FGE [12, 17] of MEQ has been coupled to an emulator of the TCV magnetic control system [18]. This latter coupling does not take transport effects into account yet (except for prescribed trajectories of selected quantities if desired). By coupling the FGE code and the emulator of the TCV magnetic control system to the ASTRA-based Fenix framework, we extend the existing TCV tools with a true flight simulator. At this point, it is worth noting that Fenix already had the SPIDER [19] and FEQIS [20] free boundary equilibrium codes available. However, to fit in with the tools commonly used for TCV, it seemed judicious to additionally couple it to FGE. On the other hand, the scope of Fenix is broader than the existing FGE-magnetic controller coupling, since it allows to simulate transport dynamics as well as to include interactions with fueling and heating actuators and kinetic control. At the moment, only minimal features are implemented for the latter in Fenix for TCV.

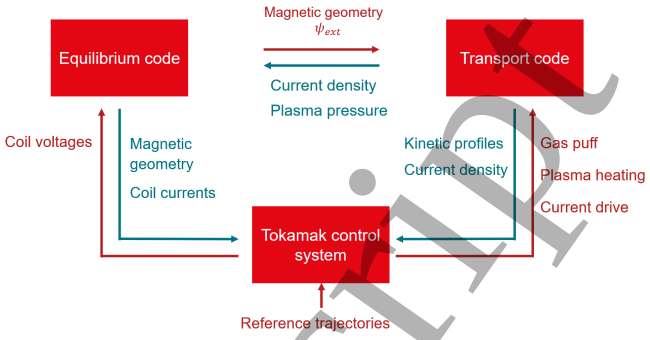

Figure 1. *Scheme showing building blocks of the Fenix flight simulator*

With the addition of Fenix, simulators integrating transport and equilibrium are now available for the main steps of discharge preparation and analysis for TCV. As a first step for discharge preparation, RAPTOR-FBT can be used to provide accurate coil current, heating, and fueling reference trajectories. Next, these references can be tested with controllers in Fenix-FGE. After the discharge was executed, LIUQE-based kinetic equilibrium reconstruction tools then allow to accurately reconstruct the plasma state that occured in the experiment.

The remainder of this paper is structured as follows. Section 2 discusses the components of the Fenix simulator for TCV and the different models that are used. Section 3 shows the convergence and benchmarking of the coupling between FGE and ASTRA. Section 4 shows the application of the Fenix flight simulator to various TCV discharges. Finally, section 5 presents conclusions and suggestions for future work.

Accepted Manuscript

2. Overview of Fenix flight simulator codes

Figure 1 shows an overview of how the different parts of the Fenix flight simulator are connected. The central component is the transport code ASTRA8 [21, 22], which solves the transport of particles, heat, and parallel current from the axis to the last closed flux surface (LCFS). The transport model used will be discussed in section 2.1. To solve these transport equations, ASTRA needs information about the magnetic geometry, which is provided by an equilibrium code solving the Grad-Shafranov equation. The main equilibrium code used in this work is the free boundary evolutive equilibrium code FGE, that is part of the MEQ suite of codes. Next to the Grad-Shafranov equation, it also evolves the circuit equations for the external conductors in time (for active coils and passive conductors). To solve the Grad-Shafranov equilibrium, information about the pressure and plasma current distribution is required, which is in turn obtained from ASTRA. The coupling scheme implemented between ASTRA and FGE is discussed in detail in section 2.2. The third component of the flight simulator is an emulator of the tokamak control system. The controller receives input about the state of the plasma and responds by sending coil voltages to the active coils to control the plasma equilibrium and by sending commands to the heating and fuelling actuators. The implementation of the TCV control system in Fenix is briefly discussed in section 2.3. This framework includes a transport code, an equilibrium code, and the controller, enabling self-consistent simulation of the tokamak plant. The only external inputs to this simulator are the reference trajectories (e.g. position of the magnetic axis, feedforward coil currents, prescribed auxiliary heating power per actuator) that the controller is ordered to track. Table 1 summarises the main models used in the different components of the Fenix flight simulator for TCV.

In terms code infrastructure, on the highest level Fenix is implemented as a Matlab-Simulink model. Within this Simulink model, ASTRA (Fortran90), FGE (octave-compatible Matlab), and the emulator of the controller (Matlab) are each wrapped inside their own Simulink block.

2.1. ASTRA transport model

The ansatz of transport codes like ASTRA is that fast parallel transport along closed magnetic field lines equilibrates most plasma quantities of interest along magnetic flux surfaces. As such, a flux-surface-averaged description is adopted in which plasma quantities vary only across flux surfaces. The main quantities which are solved for in ASTRA are the flux surface averaged density n_α and temperature T_α of charged species α, and the poloidal flux ψ. They are solved in time on a 1D radial grid from the magnetic axis to the LCFS according to the following equations:

$$\frac{\partial V' n_\alpha}{\partial t} - \frac{\dot{B}_0}{2B_0}\frac{\partial}{\partial \rho}\left(\rho V' n_\alpha\right) + \frac{\partial}{\partial \rho}\left(V'\langle(\nabla\rho)^2\rangle(n_\alpha C_\alpha - D_\alpha \frac{\partial n_\alpha}{\partial \rho})\right) = V' S_\alpha \quad (1)$$

$$\frac{3}{2}\frac{\partial V'^{5/3} n_\alpha T_\alpha}{\partial t} - \frac{\dot{B}_0}{2B_0}\frac{\partial}{\partial \rho}\left(\rho V'^{5/3} n_\alpha T_\alpha\right) + V'^{2/3}\frac{\partial}{\partial \rho}\left(V'\langle(\nabla\rho)^2\rangle n_\alpha \chi_\alpha \frac{\partial T_\alpha}{\partial \rho}\right) = V'^{5/3} P_\alpha \quad (2)$$

$$\frac{\partial \psi}{\partial t} - \frac{\dot{B}_0 \rho}{2B_0}\frac{\partial \psi}{\partial \rho} = \frac{\eta T^2}{4\pi^2 \mu_0 B_0 \rho}\frac{\partial}{\partial \rho}\left(\frac{V'}{T}\left\langle\left(\frac{\nabla\rho}{R}\right)^2\right\rangle\frac{\partial \psi}{\partial \rho}\right) - \frac{\eta V'}{2\pi\rho}(j_{BS} + j_{CD}) \quad (3)$$

In these equations, $\langle . \rangle$ represents the flux surface averaging operator, B_0 is the magnetic field at a fixed reference location R_0, $\rho = \sqrt{\phi/(\pi B_0)}$ the normalised toroidal flux radius, V' is shorthand notation for $\partial V/\partial\rho$ with $V(\rho)$ the volume enclosed within a flux surface, $G_1 = \langle(\nabla\rho)^2\rangle$, $G_2 = V'\langle(\nabla\rho/R)^2\rangle/(4\pi^2)$ with R being the major radius coordinate. C_α, D_α, χ_α, S_α, and P_α are respectively the the pinch velocity, particle diffusion coefficient, heat diffusion coefficient, volumetric particle source, and volumetric power source of species α. η is the plasma resisitivity, T the parallel current flux function, $j_{||} = \langle \mathbf{j}\cdot\mathbf{B}\rangle/B_0$ the parallel current density, $j_{BS} = \langle \mathbf{j}_{BS}\cdot\mathbf{B}\rangle/B_0$ the bootstrap current density, and $j_{CD} = \langle \mathbf{j}_{CD}\cdot\mathbf{B}\rangle/B_0$ the current density by external current drive sources. In equations 1-3, cross-channel drives for the transport (e.g. density gradients driving heat fluxes or temperature gradients driving particle fluxes) and convective heat fluxes (heat transport by convection with the particle flux) have been neglected as a modelling assumption. In general, ASTRA does have the capability to include these effects though. In this study, boundary condition values for n_e, T_e, T_i at the LCFS are imposed based on experimental data. Alternatively, options to set these values using simplified SOL models are also available in ASTRA [24, 25].

In the ASTRA model used in this work, it is assumed only deuterium (main ion species) and carbon (sputtered impurity from the wall) are present. Both ion species are lumped into a single "effective ion species" with an effective charge $Z_{eff} = (n_D + n_C Z_C^2)/(n_D + Z_C n_C)$, where n_D is the deuterium density, n_C the carbon density, and Z_C the charge state of carbon. Assuming quasi-neutrality, the densities of electrons, deuterium, and carbon are related by factors which depend solely on Z_C and Z_{eff}. In this study,

Accepted Manuscript

Table 1. Summary of the reduced Fenix model used for TCV

transport		ASTRA8 code
	equations solved	n_e, n_n, T_e, T_i, T_n, ψ
	current transport	neoclassical conductivity, bootstrap, sawtooth
	heat and particle transport	Ad hoc model inspired by Ref. [23]
	NBI	internal ASTRA model
	EC	Ad hoc gaussian deposition
	radiation	Bremsstrahlung, synchrotron, carbon radiation
	Boundary conditions	imposed n_e, T_e, T_i, T_n on LCFS ψ_{ext} on LCFS from FGE imposed neutral flux crossing LCFS from controller
equilibrium		FGE free-boundary code (from MEQ suite)
control system	magnetic control	emulation of TCV hybrid + shape controller
	kinetic control	ad hoc density control through neutral flux feedforward reference trajectories for heating

the continuity equation 1 is solved for the electron density, and the other two densities follow by assuming $Z_{eff} = 1.5$ uniform in space and constant in time. In addition, energy equations are solved for the electrons and this effective ion species according to equation 2. The poloidal flux equation 3 is also solved. In this equation, the resistivity and bootstrap current are calculated based on the neoclassical expressions in Ref. [26]. We remark that an alternative ASTRA model in which deuterium and carbon are modelled as separate species is also available. In this case, n_e and Z_{eff} follow from the transport dynamics of both species and quasi-neutrality. The formulation in which Z_{eff} is imposed is found to be easier to work with in the testing phase and to tune the model parameters. The source terms S_e, P_e, P_i, j_{CD} on the right hand side of the ASTRA equations 1-3 take contributions from ionisation (particle source), Ohmic heating, radiation (Bremsstrahlung, synchrotron radiation, and carbon line radiation), collisional ion-electron heat exchange, NBI (particle and heat source and external current drive), and EC (electron heat source and external current drive). The ionisation source is calculated by an internal 1D kinetic solver in ASTRA, assuming a prescribed flux of neutral deuterium crossing the LCFS. In Fenix, an ad hoc density controller is implemented to follow the average density trace by setting this neutral flux. The NBI deposition is also calculated by an internal ASTRA module [27], while simple Gaussian sources are used for the EC. For the external heating, feedforward time traces are preprogrammed, since no feedback controllers have been implemented for this part yet.

The model for the transport coefficients (D_e, χ_e, χ_i) in the particle and heat transport terms in 1 and 2 are inspired by the model used in the RAPTOR transport code in Ref. [28]. While the same model structure (written as a generic χ) is used for all three coefficients, the parameters in the specific formulas may vary. This model structure is composed of three contributions:

$$\chi = \chi_{ST} + \chi_{core} + \chi_{edge}. \tag{4}$$

Each of these contributions is applied in a specific zone, with the transition between the different transport coefficients in the different zones being smoothed by functions as in Ref. [29]. The particle and heat transport due to the sawtooth instability χ_{ST} is modelled by setting the diffusivity inside the $q = 1$ radius to a very large value, which effectively flattens the profiles within this radius. Thus, individual sawtooth crashes are not modelled, but their average impact is. For the current diffusion equation, sawtooth oscillations are modelled by setting a constant conductivity equal to the value at $q = 1$ inside the $q = 1$ radius, which flattens the Ohmic contribution to the current density in this region. Next, in the region between the $q = 1$ radius and the edge region chosen to start at $\hat{\rho} = 0.8$, the transport is modelled as

$$\chi_{core} = C_{ano}\hat{\rho}qT_{e,0}^{\theta} + \chi_{neo}. \tag{5}$$

In this ad hoc transport scaling taken from Ref. [28], the first term represents the anomalous turbulent transport, while the second term represents a neoclassical contribution set to be much smaller. In this expression, C_{ano} and θ are free parameters, $T_{e,0}$

Accepted Manuscript

is the maximum value of electron temperature (over the radius), $\hat{\rho} = \rho/\rho_b$ is the normalised toroidal flux coordinate with ρ_b the value of ρ at the boundary. Finally, in the edge region, chosen as $\hat{\rho} > 0.8$, the same formula of the core (expression 5) is used, but it is scaled by a factor C_{edge}

$$\chi_{edge} = C_{edge}\chi_{core}. \tag{6}$$

The values of the coefficients χ_{ST}, C_{ano}, χ_{neo}, θ, and C_{edge} that are used in this work are shown in table 2. These values were empirically tuned to get a reasonable match for around 10 Ohmic and NBI-heated TCV plasmas. Only a single H-mode discharge was included. While the resulting profiles are generally found to be relatively insensitive to the exact values of the model parameters, it would be worthwhile to develop a formal procedure to optimise these parameters over a larger database.

In order to determine whether the shot is in L-mode or in H-mode, and thus which value of C_{edge} to apply, we check if the ion heat flux crossing the separatrix $Q_{i,b}$ is larger than a limit value. In particular, we consider the discharge to be in H-mode at time t if

$$\frac{1}{\tau_{LH}}\int_{t-\tau_{LH}}^{t} Q_{i,b}dt > C_{LH}\bar{n}_e^{0.72}B_0^{0.8}S_\phi, \tag{7}$$

where $\bar{n}_e$ is the volume averaged density (in $10^{19}/m^3$), S_ϕ the toroidal surface area of the LCFS, C_{LH} a constant, and τ_{LH} a small integration time to avoid spurious oscillations which we set to 0.01s. This ad hoc scaling law was inspired by Refs. [30, 31]. It uses the exponents on the density and the magnetic field strength from Ref. [30], but incorporates the idea from Ref. [31] that the ion heat flux density ($Q_{i,b}/S_\phi$) is likely to be the crucial factor driving the transition instead of the total loss power. The coefficient C_{LH} was empirically set to 0.004. Together with the assumptions on the NBI absorption in ASTRA, this allows to match the L-H transition timing for TCV discharge 73927 (see section 4.1), which is the only H-mode discharge studied so far. To increase the predictive capability for the L-H transition, models as proposed in Ref. [16] might be implemented in the future.

The pinch velocity for the electrons C_e in equation 1 is just taken as the neoclassical Ware pinch velocity [32]. If the particle source penetration in the core is small enough, the density peaking at steady state is roughly determined by the particle convection to diffusion ratio C_e/D_e. Hence, to get realistic density profiles, we effectively set the free model parameters in such a way that we get the right C_e/D_e ratio (despite not explicitly including the turbulent contribution to the pinch velocity). In addition, we adjust the gas puff source of electrons such that we reach the intended total amount of electrons in the plasma regardless of the magnitude of D_e and C_e.

In the remainder of this paper, the transport model as described just before will be used, with the coefficients that have been reported here, unless mentioned otherwise.

2.2. ASTRA-FGE coupling

The typical challenge when coupling an equilibrium code and a transport code is to ensure that the poloidal flux profile $\psi(\hat{\rho})$ converges between both parts which each have a separate internal representation of it. In this work, a coupling scheme has been devised between ASTRA and FGE that makes the internal solutions converge to the same value by exchanging the quantities listed in table 3. Note that $\psi(\hat{\rho})$ is not transferred explicitly, but should instead converge as a result of the other quantities being exchanged. It should also be remarked that a constant offset will remain between the poloidal flux in both codes, but this has no physical significance. I.e. the reference value of the poloidal flux can be freely chosen, only variations in time and gradients in space matter.

As mentioned in the introduction already, solving the transport equations in ASTRA requires information about the magnetic field strength and the geometry, which are provided by the FGE equilibrium. Details of the exchanged quantities are given in table 3. Furthermore, Appendix A presents approximations for the asymptotic values that some of the geometric quantities reach on the axis and on a diverted separatrix.

In addition, FGE also supplies the boundary condition at the separatrix for the poloidal magnetic flux equation 3 in ASTRA. However, imposing directly the poloidal flux at the boundary would lead to a numerical instability in the coupling between the equilibrium and the transport [10, 20]. To get around this, we write the total poloidal flux as the sum of a contribution from the external conductors and a contribution from the plasma current [33].

$$L_{ext}I_p + \psi_b = \psi_{ext}, \tag{8}$$

$$I_p = \frac{1}{4\pi^2\mu_0}\frac{\partial V}{\partial\rho}\left\langle\left(\frac{\nabla\rho}{R}\right)^2\right\rangle\left.\frac{\partial\psi}{\partial\rho}\right|_b. \tag{9}$$

In these equations, I_p is the total plasma current, ψ_b is the total poloidal flux at the separatrix, ψ_{ext} is the poloidal flux at the separatrix due to the external conductors alone, and μ_0 is the vacuum permeability. With ψ_{ext}, L_{ext}, and the geometric factors in equation 9 provided from FGE, equations 8 and 9 together define a mixed boundary condition for the poloidal flux in ASTRA. This formulation of the boundary condition is stable [10, 20].

Accepted Manuscript

Table 2. Summary of the free parameters used in the Fenix transport model, tuned on TCV discharges

		$\chi_{ST}[m^2/s]$	$C_{ano}[-]$	$\chi_{neo}[m^2/s]$	$\theta[-]$	$C_{edge}[-]$
$\chi_e = \chi_i$	L-mode	40	1.5	0.02	1.2	1.0
	H-mode	40	1.5	0.02	1.2	0.2
D_e	L-mode	4	0.15	0.002	1.2	1.0
	H-mode	4	0.15	0.002	1.2	0.05

Note that while ψ_{ext} varies along the boundary, equation 8 holds for each point on the boundary. To be robust against numerical errors, we calculate ψ_{ext} and L_{ext} as an average over the N points on the separatrix in the FGE equilibrium:

$$\psi_{ext} = \frac{1}{N}\sum_{i=1}^{N} M_c(R_i, Z_i)\boldsymbol{I}_c, \tag{10}$$

$$L_{ext} = \frac{1}{NI_p}\sum_{i=1}^{N} M_p(R_i, Z_i)\boldsymbol{I}_p. \tag{11}$$

In these equations, $M_c(R_i, Z_i)$ is the inductance matrix between the conductor currents (coils and vessel) $\boldsymbol{I}_c$ and the points (R_i, Z_i) along the LCFS, $M_p(R_i, Z_i)$ is the inductance matrix between the current distribution in the plasma $\boldsymbol{I}_p$, and the points (R_i, Z_i) along the LCFS.

So, in this set-up, the total plasma current I_p is a result of the current diffusion dynamics in ASTRA, which are (to a large extent) driven by the poloidal flux at the boundary caused by the central solenoid and the other conductors as calculated in FGE. In turn, the controller actuates these coils in order to achieve a desired plasma current.

Next, we consider the inputs that FGE takes from ASTRA. To calculate the equilibrium $\psi(R, Z)$, FGE requires the basis functions $p' = \frac{\partial p}{\partial \psi}$ and $TT' = T\frac{\partial T}{\partial \psi}$ to solve the Grad-Shafranov equation [34, 35]

$$\Delta^*\psi = -2\pi\mu_0 R^2 \mathbf{j}\cdot\nabla\zeta = -4\pi^2\left(\mu_0 R^2\frac{\partial p}{\partial\psi} + T\frac{\partial T}{\partial\psi}\right) \tag{12}$$

$$\Delta^* = R\frac{\partial}{\partial R}\left(\frac{1}{R}\frac{\partial}{\partial R}\right) + \frac{\partial^2}{\partial Z^2}, \tag{13}$$

where R and Z are the radial and vertical coordinates of a cylindrical coordinate system, ζ is the toroidal angle, $\mathbf{j}$ is the current density, p is the pressure, and T is the current flux function. While FGE takes as inputs strictly p' and TT', the scheme developed here uses p', the flux surface averaged toroidal current density j_ϕ (defined as $j_\phi = R_0\langle\mathbf{j}\cdot\nabla\zeta\rangle$), and the total plasma current I_p from ASTRA to have a more accurate representation of the current density on the grid used in FGE. To ensure that the effect of artifacts in the interpolation and possible differences in the equilibrium between ASTRA and FGE (during the convergence process for example) have minimal impact, it has been found beneficial to maintain the j_ϕ profile as close as possible to the ASTRA input. To achieve this, p' and j_ϕ are first interpolated from the ASTRA $\hat{\rho}$-grid to the FGE ψ-grid using the $\psi(\rho)$ mapping from the last available FGE time step as:

$$p', j_\phi(\hat{\rho})_{ASTRA} \overset{\psi(\hat{\rho})_{FGE}}{\rightarrow} p', j_\phi(\psi)_{FGE}. \tag{14}$$

Then, the relation between $\mathbf{j}\cdot\nabla\zeta$, p' and TT' (second equality of equation 12) is flux surface averaged and used to compute TT'

$$TT' = \frac{\mu_0}{\langle 1/R^2\rangle}\left(\frac{j_\phi}{2\pi R_0} - p'\right). \tag{15}$$

The geometric factor $\langle 1/R^2\rangle$ is taken from the previous FGE time step. We remark that employing j_ϕ specifically works better than an analogous approach for $j_{||}$. This is very probably related to the additional dependence of $j_{||}$ on T itself (next to the dependence on p' and TT') that is not there for j_ϕ (see for example [36]). Finally, during the next FGE time step, I_p coming from ASTRA is used as a constraint to rescale the p' and TT' profiles. The rescaling factor is found to be very close to 1 as expected, see figure 2 in section 3.1.

Having discussed the quantities being exchanged, we now explain the iteration scheme between both codes. A simple time-stepping approach is followed, in which ASTRA and FGE run iteratively one after the other, always taking the latest available output from one another. Both codes run with the same time step Δt, which is chosen to be the time step of the TCV magnetic controller $\Delta t = 0.1$ms [37]. Hence, it can be imagined that both codes run on staggered time grids that are shifted by $\Delta t/2$ with respect to each other. In the middle of the cycle, the iteration scheme looks as follows:

- FGE runs for $[t_0 - \Delta t, t_0]$, based on ASTRA basis functions at time $t_0 - \Delta t/2$
- ASTRA runs for $[t_0 - \Delta t/2, t_0 + \Delta t/2]$, based on FGE geometry at time t_0
- FGE runs for $[t_0, t_0 + \Delta t]$ based on ASTRA basis functions at time $t_0 + \Delta t/2$
- etc.

To initialise this iteration scheme, a two-step approach is followed. During a first short period (0.03s), ASTRA

Accepted Manuscript

is run on an initial MEQ equilibrium that is kept constant to allow the first ASTRA transients to settle. (A very basic artificial controller inside ASTRA makes sure the plasma current stays at the appropriate level during this period when there is no input for ψ_{ext}.) Then, the previously described iteration scheme is started, but during a second short period (0.02s), the profiles coming from ASTRA are relaxed in time before going into the FGE equilibrium. The goal of this is to facilitate a smooth convergence process between both codes. After these 0.05s, profiles and geometry are exchanged without further relaxation.

When run at the controller frequency of 0.1ms, this scheme works well and the solutions of ASTRA and FGE converge quickly. Note that after the initialisation phase, no more convergence iterations are needed between ASTRA and FGE, i.e. to advance the simulation in time by Δt just one call to ASTRA and one call to FGE are needed, making this scheme very fast.

2.3. TCV controller

In order to realistically model the evolution of the free boundary equilibrium described in the previous section, Fenix has been coupled with an emulator of the TCV magnetic control system [18]. The standard TCV controller, called "hybrid" controller for historical reasons, controls the radial and vertical position of the plasma and the total plasma current in feedback (RZIp control), while the plasma shaping is done through the feedforward trajectories programmed for the poloidal field coils [37]. Recently, a shape controller has been developed for TCV which also controls the separatrix shape in feedback [18]. It features an additional feedback loop around the hybrid controller which sends RZIp and poloidal field coils references to the latter in order to achieve the desired shape. Both the hybrid controller and the shape controller are implemented in the emulator coupled to Fenix.

As mentioned in section 2.1, only feedforward traces traces for NBI and EC heating and current drive are considered for now, while an ad hoc controller is implemented on the gas puff to track the desired electron content of the plasma.

For now, no specific observers are implemented and the controllers receive perfect information about the plasma state. In particular, the hybrid controller receives magnetic probe and flux loop measurements without any noise added, while the shape controller additionally receives the exact equilibrium state and not the state from magnetic equilibrium reconstruction as in real TCV experiments.

3. Benchmarking

This section presents results proving the successful coupling between Fenix-ASTRA and FGE which has been discussed in section 2.2. First, it is shown that ASTRA and FGE converge to the same equilibrium in section 3.1, after which section 3.2 compares results with this coupling to the ASTRA-SPIDER coupling also available in Fenix.

This section considers the 280kA Ohmic L-mode TCV discharge 83448 as a test case, which is simulated from ramp-up to ramp-down. The equilibrium is limited on the inboard side until 0.4s after which it becomes diverted until 1.25s at which point it becomes limited on the inboard side again. Notably, the shape controller is active from 0.7s to 1.2s, whereas outside this interval, only the RZIp-hybrid controller is on (see section 2.3).

3.1. ASTRA-FGE convergence

The poloidal flux profile $\psi(\hat{\rho})$ is the most interesting quantity to consider when verifying the convergence between ASTRA and FGE. Recall that both codes have a separate internal representation of it, which should converge as a result of the quantities listed in table 3 being exchanged. The left column of plots in figure 2 shows that the poloidal flux difference between the separatrix and the magnetic axis is almost exactly the same in ASTRA and FGE. The middle plot zooms in on the initial phase in which the values converge after a short transient. The bottom plot zooms in on the main flattop phase. The shaded areas represent the time window during which the initialisation procedure allowing a smoother convergence between ASTRA and FGE is active (see section 2.2). In the yellow shaded area, the equilibrium is kept fixed, while during the purple shaded area the profiles going from ASTRA to FGE are undergoing a relaxation in time.

It can be seen that a slightly larger difference in fluxes occurs during the diverted phase. This is most likely due to the treatment of the values of the geometric profiles close to the separatrix for such diverted conditions. This difference remains very low though, never exceeding 1% of the FGE value. The two bottom plots in the right column of figure 2 show the radial profiles of $\psi(\hat{\rho})$ at a limited and a diverted time slice respectively. Again, it can be seen that the profiles agree very well between ASTRA and FGE. Note that the constant offset between the ASTRA and FGE fluxes was removed by deducting the value of the flux at the magnetic axis in these two plots. Lastly, the top right plot in figure 2 shows the rescaling factor used on the p' and TT' functions during the FGE time step to make sure that the current in FGE matches the one from ASTRA. It can be seen that this correction

Accepted Manuscript

Table 3. Quantities exchanged in the coupling between transport (ASTRA) and free boundary evolutive equilibrium (FGE)

FGE → ASTRA	T, $\partial V/\partial\rho$, $\langle(\nabla\rho)^2\rangle$, $\langle(\nabla\rho/R)^2\rangle$, $\langle 1/R^2\rangle$, $\partial\rho/\partial a$, B_0	metric quantities in transport equations
	$R_{geom}(\hat{\rho})$, $Z_{geom}(\hat{\rho})$, $a(\hat{\rho})$, $\kappa(\hat{\rho})$, $\delta(\hat{\rho})$, $V(\hat{\rho})$, limited/diverted equilibrium (boolean)	possible use in transport models
	ψ_{ext}, L_{ext}	boundary condition for ψ equation
ASTRA → FGE	$p'(\hat{\rho})$, $j_\phi(\hat{\rho})$, I_p	basis functions for the equilibrium

generally remains below 1%, again indicating a good convergence between both codes. Note that the spike around 1.25s coincides with the diverted to limited transition, at which time Fenix struggles to keep the equilibrium stable (see also the strong oscillations in the plasma current in figures 3 and 7). It could be argued that a very brief spike to only 10% deviation in such a difficult phase of the simulation indicates robust convergence properties.

3.2. SPIDER-FGE benchmark

As mentioned before, Fenix already includes the SPIDER [19] and FEQIS [20] equilibrium codes, which can both be run in free boundary or in prescribed boundary mode. In this section, we benchmark the newly developed Fenix-FGE coupling with a simulation using SPIDER. A prescribed boundary has been assumed, since the TCV coils geometry has not yet been implemented in SPIDER or FEQIS. All the settings are identical in both simulations, except for the equilibrium. The separatrix shape used in SPIDER is taken from the Fenix-FGE simulation sampled at 0.1s. Also, an ad hoc controller on ψ_{ext} is used in the Fenix-SPIDER run to track the plasma current trace from the Fenix-FGE simulation, again sampled at 0.1s. Hence, while the equilibrium and the plasma current are dynamically evolving in the Fenix-FGE simulation, these dynamics are expected to be more limited and different in the Fenix-SPIDER simulation.

Figure 3 shows a comparison between both simulations in terms of flux map $\psi(R,Z)$, $\frac{\partial V}{\partial\rho}$ as an example of a geometric profile calculated in the equilibrium code coupled to ASTRA, $j_{||}$ as one of the kinetic profiles calculated by ASTRA on the provided geometry, and the time trace of the plasma current. The left column shows these quantities for a limited time slice, while the right column shows a diverted time slice. For the limited time slice, the results are almost identical between Fenix-FGE and Fenix-SPIDER. The slight difference on the current density profile is likely due to some transient behaviour that is not represented in the Fenix-SPIDER case. For the diverted time slice, there is a difference in $\frac{\partial V}{\partial\rho}$ near the edge. For Fenix-FGE, the value at the diverted edge is calculated using the limits described in Appendix A. While the value at

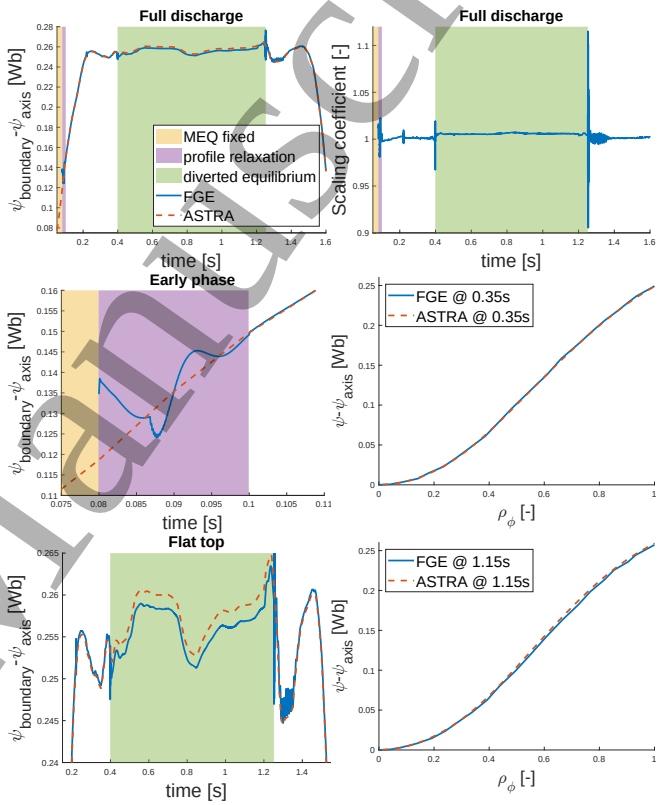

Figure 2. *Illustration of convergence between FGE (red) and ASTRA (blue) for a Fenix simulation of TCV discharge 83448. The time intervals during which the equilibrium is kept fixed (yellow shade), during which the profiles going from ASTRA to FGE are relaxed in time (purple shade), and during which the equilibrium is diverted (green shade) are also indicated. Left column shows the difference between the poloidal flux at the boundary and on the axis. Right column first shows the scaling coefficient on p' and TT' profiles coming from ASTRA used in FGE and then the poloidal flux profile.*

the separatrix is supposedly exact, numerical tests with the MEQ code showed that the observed decrease in $\frac{\partial V}{\partial\rho}$ only occurs very close to the separatrix. However, due to the relatively coarse radial grid used in ASTRA, the region over which the separatrix value influences the profile is artificially extended.

To further investigate the influence of this, the same Fenix-FGE simulation is ran again, but with the

Accepted Manuscript

separatrix value of the geometric profiles taken from a simple linear extrapolation during diverted time slices instead of using the analytical relations§. For this case, shown in yellow in figure 3, $\frac{\partial V}{\partial \rho}$ is much closer to the value from the FENIX-SPIDER case at the separatrix. Despite the differences in geometric profiles near the edge, the kinetic profiles and $\psi(R, Z)$ agree well between the three cases. For other geometric and kinetic profiles, similar results are observed. Lastly, it needs to be mentioned here that the geometric profile near the boundary in prescribed boundary SPIDER is not per se perfectly correct either. Prescribed boundary SPIDER only solves the equilibrium up to $\frac{\psi-\psi_b}{\psi_m-\psi_b} = 0.995$ and the presence of the X-point is only described through the separatrix shape (which is provided with a finite number of points). Even though small difference exist between Fenix simulations with FGE and SPIDER respectively, we consider the results to be in good agreement with each other.

Lastly we comment on the computational cost of these Fenix simulations. The simulations reported in this paper have been run on the SPC-lac10 computing cluster on Intel(R) Xeon(R) Silver 4214 CPUs. Running on a single thread, the default Fenix-FGE case shown in figure 2 and in red in figure 3 took 2714s to run the 15500 time to simulate the discharge from 0.05s to 1.6s. Around 75% of the computational was spent on FGE and the Simulink block wrapping it. The equivalent Fenix simulation using SPIDER prescribed boundary (blue in figure 3) only required 613s. This much shorter runtime is explained by the fact that a much simpler equilibrium problem is solved in this case. These numbers are representative for all the Fenix-FGE simulations shown in this paper, except the simulation with TGLF in section 4.4. This simulation used 8 parallel processes for the TGLF part and completed in 18762s of wall time.

4. Application to TCV cases

This section highlights the usefulness and gives an indication of the validity of Fenix by applying it to a number of selected TCV discharges. Section 4.1 considers an NBI heated H-mode case, section 4.2 presents a discharge in which the shape controller was used, and section 4.3 investigates a series of discharges in which the triangularity is scanned.

4.1. H-mode case 73927

The first case considered is a diverted, NBI-heated, ITER baseline (IBL) scenario for TCV [38, 39]. Figure 4 shows a number of characteristic time traces

§ At the separatrix, we set $\langle 1/R^2 \rangle = (4\pi R_0^2 B_0 \rho_b)/(TV') = 1/R_X^2$ for consistency of the equilibrium instead of extrapolating for this quantity.

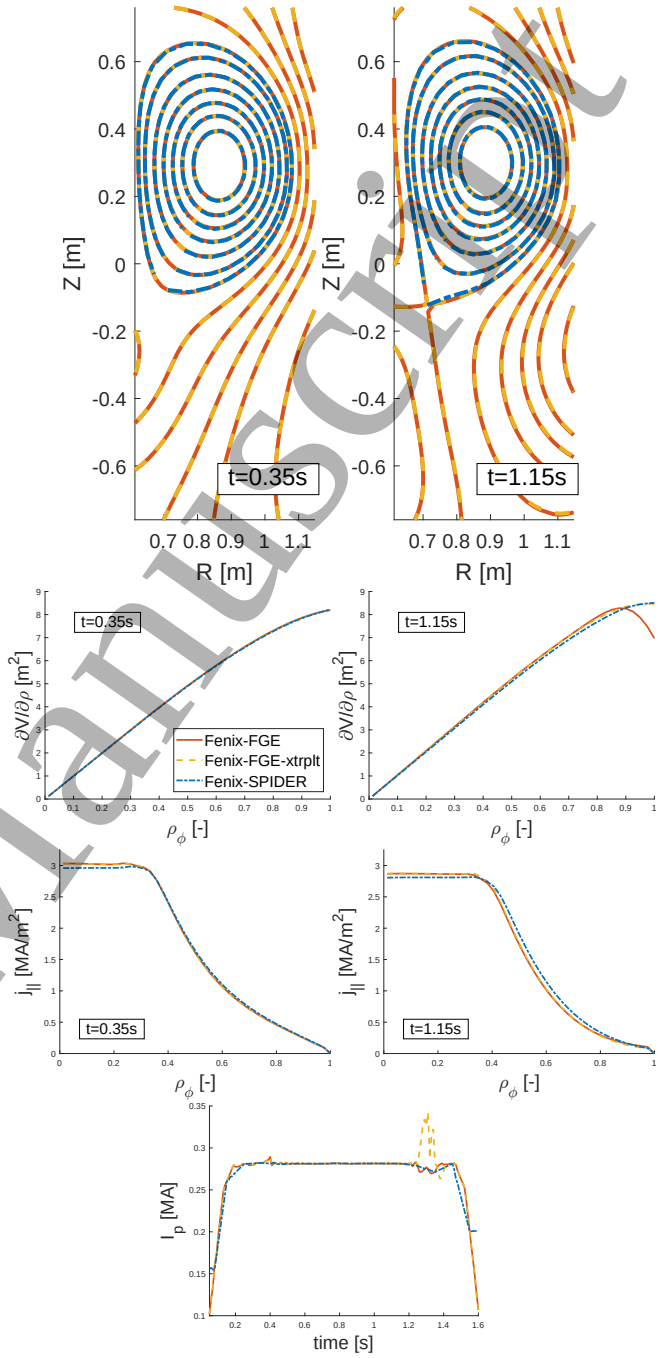

Figure 3. *Comparison of Fenix simulations for TCV discharge 83448. Default Fenix simulation with FGE, using analytical relations for the metric coefficients at the diverted separatrix in ASTRA (red); simulation with FGE but using an extrapolation to set the metric coefficients at the diverted separatrix (yellow); simulation with SPIDER prescribed boundary equilibrium solver in blue. Left column shows the early limited phase, right column shows the later diverted phase.*

Accepted Manuscript

for this discharge, comparing the kinetic equilibrium reconstruction (KER) to Fenix simulations. It can be seen that the plasma current is ramped up to 220kA in two steps, with the NBI power being ramped up to 1.1MW during this second step as well. As the NBI power increases, the plasma goes into H-mode around 0.73s and transitions back to L-mode around 1.65s shortly after the NBI is turned off. For this discharge, only the hybrid magnetic controller was active. The KER results (in blue) used to represent the experiment in this study are always based on the LIUQE-ASTRA-based framework described in Refs. [12, 14]. The "nominal" Fenix simulation using the models and settings described in section 2.1 is shown in red. The other simulations show the influence of moderate changes in the model parameters. These variations include narrowing the pedestal to $\hat{\rho} > 0.85$ (from 0.8, simulation in yellow), a reduction of the NBI absorbed power to 50% (from 65%, simulation in purple), and an increase in Z_{eff} to 1.75 (from 1.5, simulation in green).

Comparing the time traces between KER and the Fenix simulations in the figure, it is clear that, with the chosen parameters in the ad hoc transport models, Fenix captures the experimental traces very well. The L-H transition timing, indicated by the red shaded area for the default Fenix simulation, also matches the experimental timing very well. Note that the C_{LH} governing the H-mode entry is not changed from one simulation to another, which results in the low-NBI absorption case entering H-mode late. The increased fluctuations on the plasma current in KER are due to ELMs disturbing the equilibrium and its reconstruction, while these are not modelled in Fenix. The central solenoid current, which is the main actuator used to control the plasma current, is matched very well in L-mode, while in H-mode it ramps up too slowly for the default Fenix simulation. The simulations with parameter variations show that this match can be further improved by increasing Z_{eff} or reducing the electron temperature (through reducing confinement or reducing the heating), both of which increase the plasma resistivity.

The small difference in injected NBI power is due to the diagnostic NBI that is not included in Fenix. Furthermore, the absorbed power is scaled down to 65% in the standard Fenix simulation with respect to the value calculated by the internal ASTRA NBI module. This is done to bring it closer to the absorbed power found in KER. Inherently, this difference is due to the neutral concentration being higher in KER than in Fenix, which causes higher charge-exchange losses in KER. In general, this neutral concentration is not well known in TCV, leading to significant modelling uncertainty in the NBI absorption. A different solution

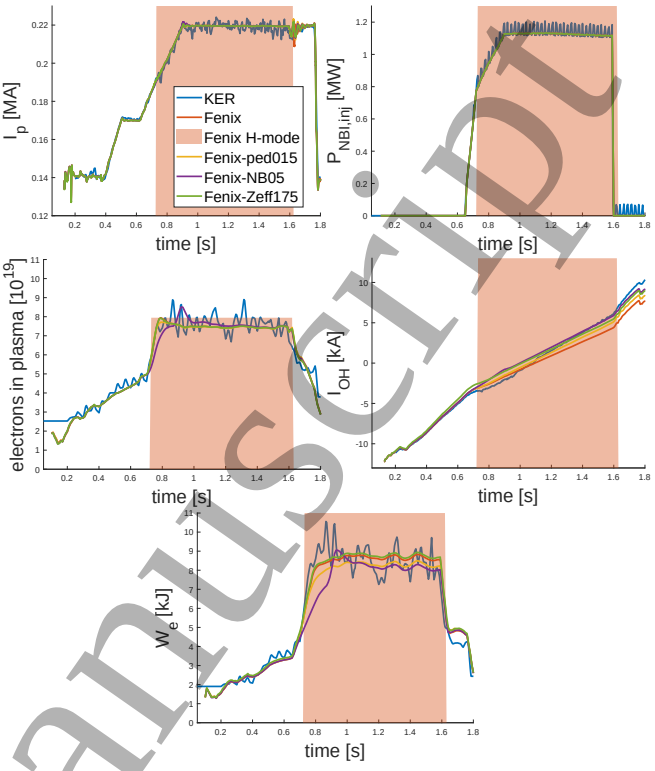

Figure 4. *Comparison of time traces between Fenix simulations and kinetic equilibrium reconstruction for TCV discharge 73927.*

to avoid this downscaling of the absorbed power would be to multiply the electron diffusion and convection coefficients by a certain factor, which would also require the electron source and therefore the neutral concentration to be higher to establish the same electron content in the plasma (which is feedback controlled).

To complement the time traces shown in figure 4, figures 5 and 6 show the electron temperature profiles, the coil currents, and the poloidal flux map $\psi(R, Z)$ for selected time slices of the nominal Fenix simulation. Results are shown for a time slice in the early limited phase, a diverted time slice before the NBI comes on, and a diverted time slice during the NBI-heated H-mode flattop phase. The left column of plots in figure 5 shows that the electron temperature in Fenix corresponds well with KER and with the Thomson Scattering (TS) data (which KER is based on). It needs to be mentioned that this match is a bit less convincing for the limited time slice at 0.3s. The right column of plots in figure 5 shows that also the current in the poloidal field coils used for shaping are pretty close between KER and Fenix. (The E coils are located on the high field side and the F coils on the low field side. We refer to Ref. [40] for a description and a figure of the TCV coil geometry.) As a result, also the flux maps shown in figure 6 agree well between KER

Accepted Manuscript

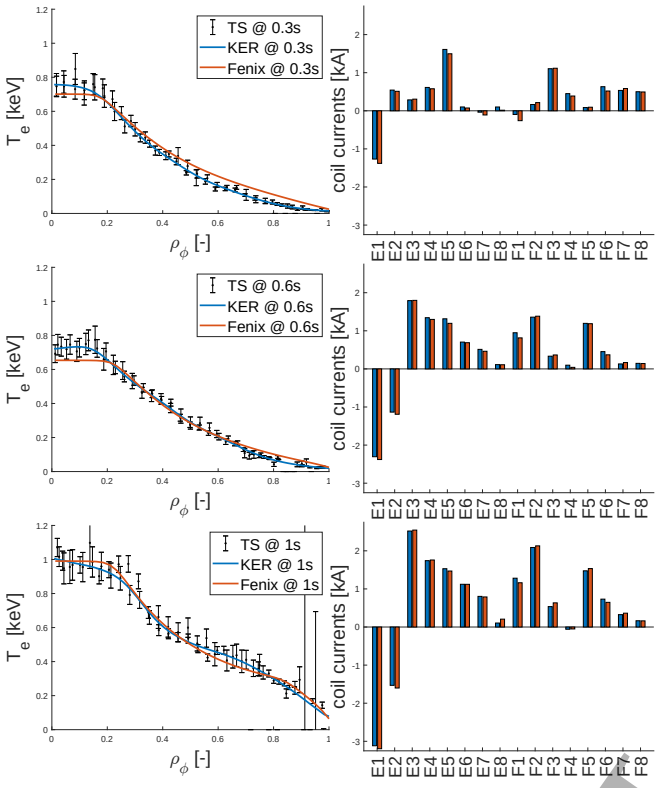

Figure 5. *Comparison of temperature profiles and coil currents at selected time points between the nominal Fenix simulation and kinetic equilibrium reconstruction for TCV discharge 73927.*

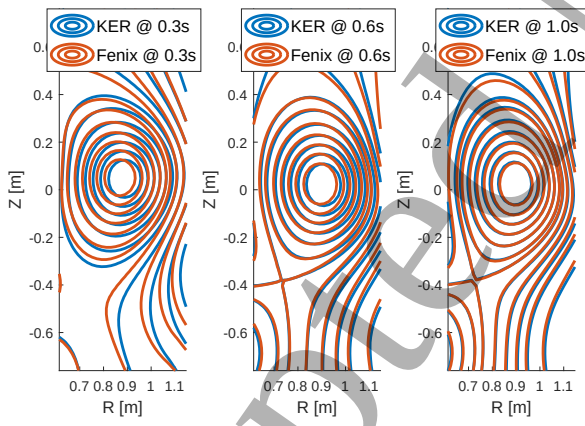

Figure 6. *Comparison of poloidal flux maps at selected time points between the nominal Fenix simulation and kinetic equilibrium reconstruction for TCV discharge 73927.*

and Fenix. There is clearly a larger difference in the first equilibrium, which is most likely due to the kinetic profiles being less accurate.

This proof of principle convincingly demonstrates the capability of Fenix to reproduce the behaviour of both the equilibrium and the kinetics in a full TCV discharge. The validation of this model and the model parameters over a large dataset is left for future studies.

4.2. shape controller case 83448

This section demonstrates the capability of Fenix to test different controllers. To this end, the Ohmic L-mode TCV discharge 83448 that was already considered in section 3 is revisited. We compare the experimental data from KER with two Fenix simulations. One Fenix simulation uses the magnetic shape controller between 0.7s and 1.2s as in the experiment, while the second simulation only uses the hybrid magnetic controller. Otherwise, both Fenix simulations use identical settings, i.e. those described in section 2.1. Hence, the same physics model with the same parameters are used as in the "nominal" simulation of the IBL discharge discussed in section 4.1.

Figure 7 shows that both Fenix simulations manage to replicate the electron particle content and thermal energy pretty well. Also, the plasma current in the simulations tracks the reference very well, except during the transition from a diverted back to a limited equilibrium, which creates oscillations in the controller that were not observed in the experiment. On the other hand, from 0.8s on an offset appears between the plasma current in the experiment and the plasma current reference trajectory the controller aims to track. This offset is created by the dynamics of the central solenoid when it passes the zero current state. In the experiment, the controller apparently ignores this small offset after this zero-crossing and the offset persists. This zero-crossing behaviour of the central solenoid is not modelled in the FGE equilibrium code and the controller does track the reference trajectory in the Fenix simulation, explaining the a difference between experiment and simulation. For all these time traces, the difference between the Fenix simulation with and without the shape controller is small. Nonetheless, the shape controller does bring the shape closer to the reference, as it is seen from the projected errors in the bottom right plot, which shows the time traces of the errors on the different shape components that the shape controller is trying to bring to zero. During the shape control phase, those errors are lower for the simulation with shape controller. Moreover, the errors observed from equilibrium reconstruction are also driven to lower values during this shape control phase. This confirms that the shape controller did have an effect during the experiment, and that his effect is reproduced in the Fenix simulation.

To analyse this further, figure 8 shows the equilibrium during a time step before the shape controller was activated and a time step when it has been active for some time. In the earlier time slice, both Fenix simulations are identical, but for the shape controlled phase, the equilibrium with shape

Accepted Manuscript

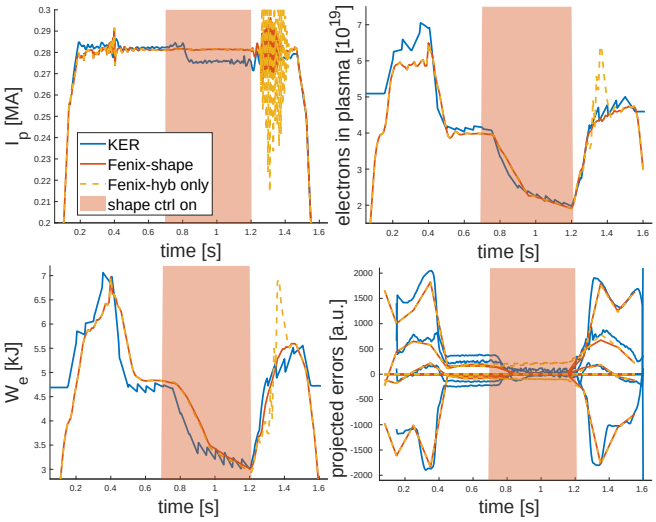

Figure 7. *Comparison of time traces between Fenix simulations and kinetic equilibrium reconstruction for TCV discharge 83448. Note that the vertical axis does not start at zero in the top two and bottom left plots to better highlight the variations.*

controller is slightly closer to the KER and closer to the shape control reference points which are indicated by black dots in the right plot. Finally, the bottom plots in figure 8 show that the experimental electron temperature profile and coil currents are well matched by the Fenix simulations, and that the difference is small between the two Fenix simulations. This case nicely illustrates that Fenix is capable of capturing the subtle differences in equilibrium shape obtained with different magnetic controllers.

4.3. Marginal stability during triangularity scans

In this section, we investigate a series of lower single null Ohmic L-mode triangularity scan experiments. The starting point of this series is TCV discharge 68783 [41], which varies the top triangularity stepwise from -0.6 to +0.6. The bottom triangularity is kept approximately constant at 0.25 and the plasma current is kept at 180kA. Recently, discharge 87688 attempted to repeat this discharge, but disrupted in a vertical displacement event during the first triangularity interval. In order to have the discharge succeed, the target safety factor on axis was increased (lowering the expected internal inductance l_i) during the shot preparation for discharge 87697. This reduced the elongation during the discharge and hence reduced the growth rate of the vertical instability. This experience shows this scenario to be marginally stable, making it an interesting case to investigate with Fenix.

Since the reduced transport models in Fenix do not capture confinement variations with (negative) triangularity, we consider "interpretative" Fenix simulations in this section. This means Fenix still solves the free boundary equilibrium evolution driven by the controller as well as the current diffusion equation, while the electron density, electron temperature and ion temperature are set based on experimental data. The electron density and temperature are set to match the profiles obtained from Thomson Scattering, while the ion temperature is set to 70% of the electron temperature as an approximation. For these Ohmic discharges, this scaling of the electron temperature is reasonably close to the ion temperature measurements from charge exchange recombination in the time windows where they are available.

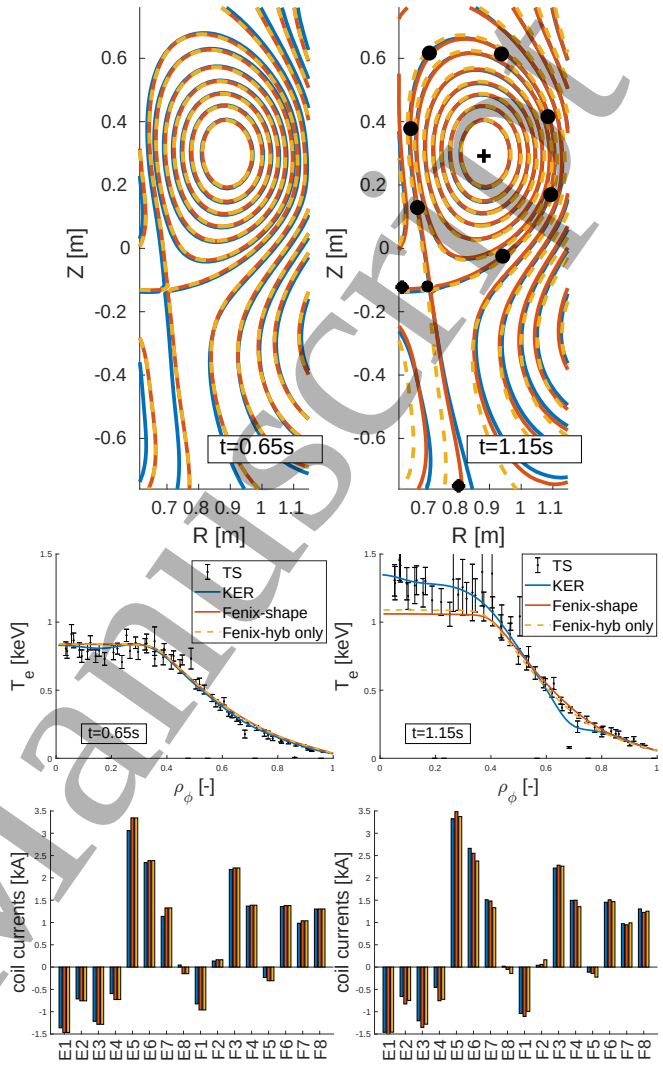

Figure 8. *Comparison of flux maps, temperature profiles and coil currents at selected time points between kinetic equilibrium reconstruction (blue), Fenix simulation with shape controller active as in the experiment (red), and Fenix simulation with the shape controller disabled (yellow) for TCV discharge 83448.*

Figure 9 compares the recent discharge 87688

Accepted Manuscript

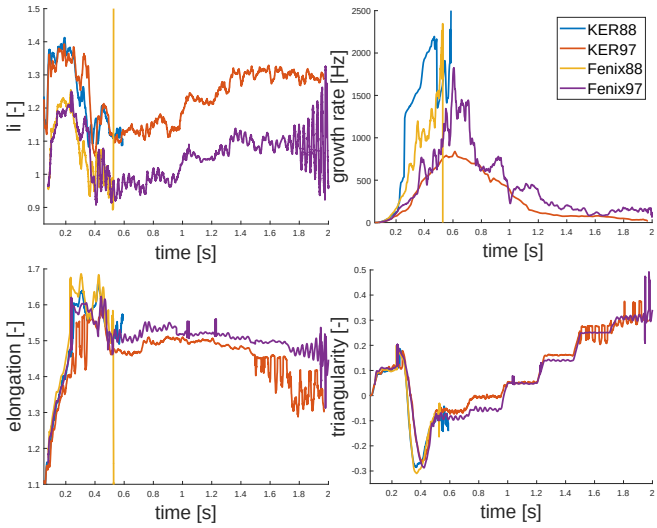

Figure 9. *Comparison of selected time traces for TCV discharges 87688 and 87697 between interpretative Fenix simulations and kinetic equilibrium reconstruction. Note that the origin is not included in the left two plots to better highlight the variations.*

which disrupted around 0.6s and discharge 87697 that did run through. Comparing the KER time traces for both shots, a modest but nonetheless significant difference in elongation is indeed present around the time at which 87688 disrupts. This leads to higher growth rates for discharge 87688 and to a disruption. To reproduce this behaviour in Fenix, it was necessary to impose a peaked spatial profile of $Z_{eff} = 1+2.5(\hat{\rho}-1)^2$, which leads to a more peaked current profile. This recreates the behaviour of 87688 disrupting at a time close to the experimental disruption time, while 87697 runs through. In case a flat Z_{eff} profile is applied, both discharges would run through. This peaked profile is justified by the observation that the old discharge 68783, programmed identically to 87688, did run through. The lower loop voltage in the old discharge indicates different machine conditions and impurity penetration. Our simulations thus help explaining why rerunning the same shot several months later did not work as expected. Lastly, it is worth commenting on what is going on in the late phase of 87697. In the experiment, the equilibrium started oscillating between diverted and limited by touching the outer wall. In the Fenix simulation, the elongation at the end of the simulation is still higher and the plasma does not start touching the wall. On the other hand strong oscillations originate, which are due to the plasma current controller not being well tuned for this shape.

While it is clearly a nuisance to have to tweak details of the simulation set-up such as Z_{eff} to reproduce the experiments, it also shows that kinetic effects can be important for the equilibrium and stability of the discharge. This highlights the importance of flight simulators like Fenix that couple equilibrium and transport to test discharge scenarios and controllers. In particular, Fenix allows to asses their robustness to changes in modelling assumptions corresponding to physics uncertainties.

Another way to stabilise this marginal discharge could have been to use the shape controller. In fact, if the shape is controlled, it should not be sensitively affected by changes in the kinetic profiles, allowing for a safer operation and avoiding intolerable vertical instability growth rates. This is tested in simulation in figure 10, which compares the preprogrammed traces from the shot preparation (FBT), the kinetic equilibrium reconstruction (KER), the Fenix simulation with the hybrid controller as used in the experiment (same data as in figure 9), and finally a Fenix simulation in which the shape controller is activated at 0.35s. The first observation is clearly that for all the other settings kept the same, Fenix with the shape controller runs through until the end of the simulation time at 0.8s. While the differences in the triangularity and elongation seem small, there is an appreciable difference in the growth rate of the vertical instability nonetheless. It is also worth noting that the triangularity is not perfectly controlled to its target value in the first interval. This can be because the controller is struggling with the challenging shape, but could also be an artifact of the specific points of the shape that are controlled. I.e. even if a small set of selected shape points is controlled perfectly, the separatrix shape still has some degrees of freedom to deviate from the full intended shape and thus to change shape parameters such as elongation and triangularity.

To take this exercise of using the shape controller a step further, we also applied it in a simulation of the full 87697 discharge. Results of this are shown in figure 11. Here it is interesting to remark that the internal inductance l_i used for the shot preparation is much lower than the values found in KER and in the Fenix simulations. This is due to the intentional "misprogramming" of the shot to force a reduced elongation in the experiment. This misprogramming did indeed lead to the elongation being lower than the value in the shot preparation for the experiment and for the Fenix-hybrid simulation. On the other hand, when the shape controller is active, it compensates for this "erroneous" assumption on the kinetic profiles during the shot preparation and maintains the elongation much closer to the intended value. Nonetheless, the triangularity does not quite follow the shape reference towards the end of the discharge.

Accepted Manuscript

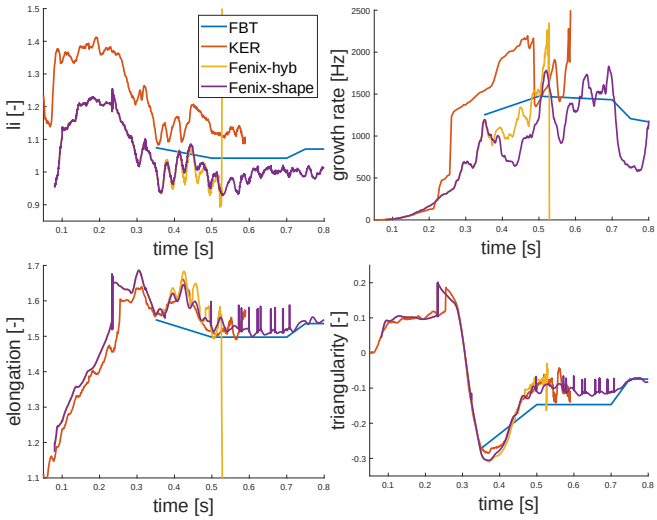

Figure 10. *Comparison of selected time traces for TCV discharges 87688 between shot preparation (FBT), kinetic equilibrium reconstruction (KER), and interpretative Fenix simulations with and without shape controller. Note that the origin is not included in the left two plots to better highlight the variations.*

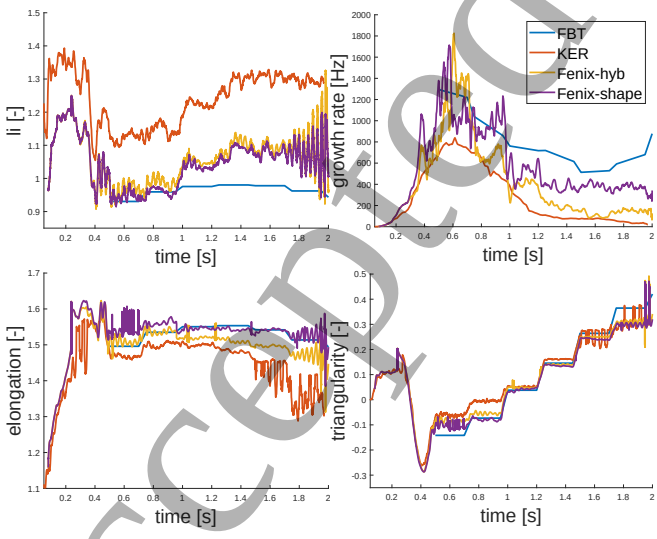

Figure 11. *Comparison of selected time traces for TCV discharges 87697 between shot preparation (FBT), kinetic equilibrium reconstruction (KER), and interpretative Fenix simulations with and without shape controller. Note that the origin is not included in the left two plots to better highlight the variations.*

4.4. Improved transport description using TGLF

Thanks to Fenix incorporating ASTRA, also the more elaborate transport models from ASTRA are available. In this section, we run Fenix with the TGLF quasi-linear transport model [42] for TCV discharge 83448 that was already studied in sections 3 and 4.2. TGLF is run in Miller geometry for the electron, deuterium, and carbon species. Saturation rule 2 is used, with the electromagnetic effects causing magnetic fields perpendicular to the background magnetic field included but those creating magnetic fields parallel to it disabled. This way, it provides the turbulence-driven contribution to the transport coefficients D_e, χ_e, χ_i and C_e instead of the ad hoc transport model used before (see section 2.1). (Note that TGLF inherently takes the cross channel transport effects that were neglected before into account as well.) Theoretical expressions for the neoclassical contributions [26] are added to these, while the sawtooth model used before is maintained. For the L-mode case studied here, we use TGLF over the full radius with 40 points uniformly spaced from $\hat{\rho} = 0$ to $\hat{\rho} = 1$ at a time resolution of 4ms. Boundary conditions are still taken from the experimental data. In ASTRA, Z_{eff} is still imposed externally. Nothing is changed for the current transport w.r.t. the model described before.

It was found that a maximum in density near the separatrix tends to develop in the diverted phase, which can also disturb the profiles further inward. To suppress this issue, the controller gain for the density feedback was reduced, the injection energy of the neutrals was increased to have a broader ionisation source, and the value of the geometric profiles at the diverted separatrix was taken from a simple extrapolation to avoid the minimum at the separatrix that tends to occur when using the asymptotic values described in Appendix A. Otherwise, no changes were made to the controller or to the coupling with the equilibrium.

Results of this Fenix-TGLF simulation are shown in figures 12 and 13, compared to the equilibrium reconstruction and the Fenix simulation with the ad hoc transport model used before. The shape controller is active in both Fenix simulations, as it was in the experiment. The time traces shown in figure 12 clearly feature more fluctuations for the Fenix-TGLF simulation. This is explained by the transport coefficients constantly adjusting to changes in gradients, equilibrium shape, and fueling, thus inhibiting to reach a fully stationary solution. Despite the increased fluctuation level, the overall trends are still very similar. The density control still manages to keep the electron content in the plasma close to the reference, while the magnetic controller does the same for the plasma current, position, and shape.

Accepted Manuscript

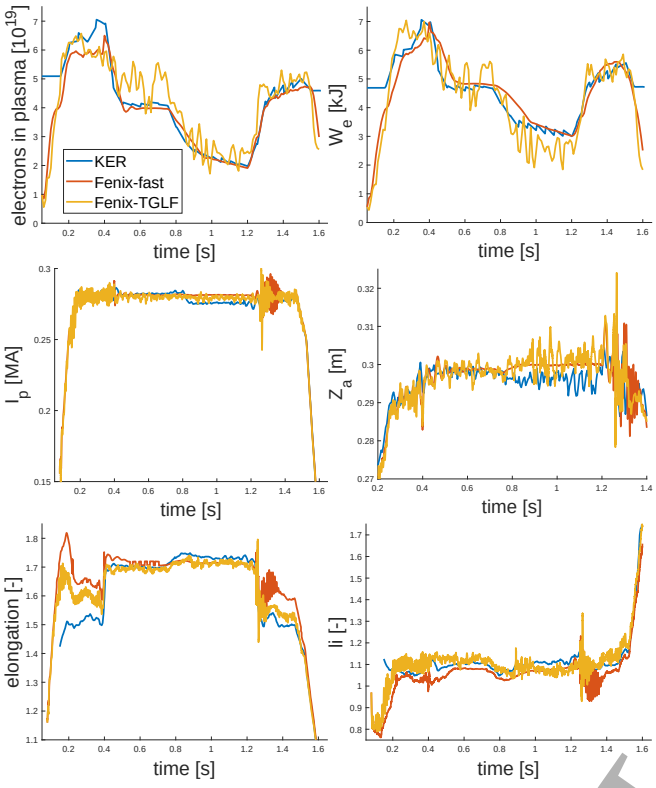

Figure 12. *Comparison of selected time traces for TCV discharges 83448 between kinetic equilibrium reconstruction (KER), Fenix simulations with the ad hoc transport model and TGLF respectively. Note that the origin is not included in the bottom four plots to better highlight the variations.*

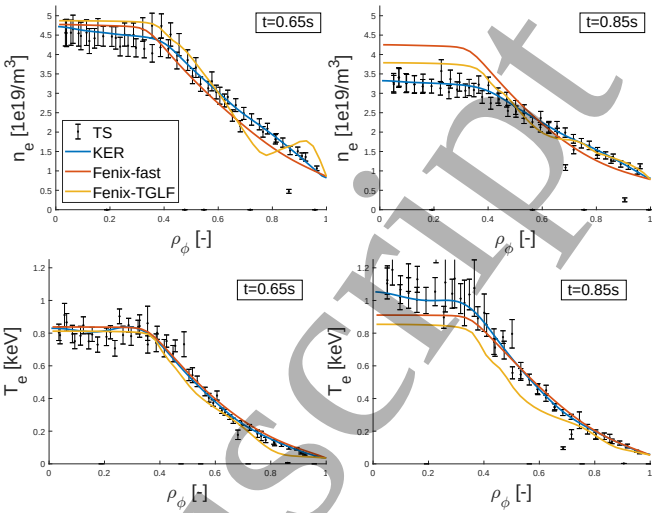

Figure 13. *Comparison of electron temparature and density profiles at selected times for TCV discharges 83448 between kinetic equilibrium reconstruction (KER), Fenix simulations with the ad hoc transport model and TGLF respectively.*

Most notably, without any need for parameter tuning, TGLF gives an accurate estimate of the thermal electron energy content, consistent with full radius TGLF simulations on ASDEX-Upgrade [43]. Figure 13 focuses on the density and temperature profiles for selected time slices. The time slice at 0.65s is selected to show the spurious local maximum of the density profile near the separatrix that persists at certain times despite our efforts to suppress them. This results in the temperature being too low in this region. At 0.85s, the density and temperature profiles look regular and are close to the experimental data.

5. Conclusions

This paper shows the application of the Fenix flight simulator, originally developed for the ASDEX Upgrade tokamak, to a new tokamak, TCV. In particular, Fenix has been coupled to the FGE evolutive free boundary code of the MEQ code package, which is widely used for the preparation and analysis of TCV discharges. Furthermore, the TCV magnetic controllers were coupled to Fenix, enabling simulations of full TCV discharges incorporating transport dynamics coupled to free boundary equilibrium driven by the real TCV controllers.

The new and simple coupling scheme proposed here between ASTRA (the transport code at the basis of Fenix) and FGE converges in time and runs smoothly and stably at the frequency of the TCV magnetic controller without needing additional convergence iterations at every time step. This coupling has been benchmarked and the convergence between FGE and ASTRA proven. For the transport modelling, reduced models are presented that are a synthesis of models that were already in Fenix and transport models in use for TCV and other tokamaks, notably in the RAPTOR code.

Various TCV discharges are modelled with Fenix, demonstrating its capacity to give close indications about the expected behaviour of the discharge, both in terms of magnetic equilibrium and kinetic profiles. Given that the intended use of the Fenix flight simulator is to check discharge designs and to validate and develop controllers, the focus was on testing the influence of different controllers. In addition, the presented cases also showed the dependence of the equilibrium and its stability on the kinetic profiles, thus indicating the relevance of coupling transport and equilibrium codes. With this article, transport-equilibrium couplings are now in place for TCV for discharge and controller validation (Fenix), discharge design (RAPTOR-FBT), and discharge reconstruction (KER).

In future work, Fenix should be applied to a larger pool of discharges to further validate the transport

Accepted Manuscript

models that are used and to identify gaps in the physics that need to be addressed. In particular, ECCD-heated discharges are yet to be investigated. In addition, it would also be interesting to investigate neural network transport models based on higher fidelity codes such as TGLF-NN. Other physics elements that would be most interesting to add would be an improved pedestal model and improved models for the SOL and fueling. This would additionally allow to bring controllers for divertor conditions and detachment in the scope of Fenix. On the control side, it would be instructive to also implement realistic kinetic controller algorithms for TCV. Furthermore, the fidelity and robustness of the framework could be improved by also incorporating realistic measurement noise, observers, and synthethic diagnostics.

Lastly, Fenix has so far only been applied post-discharge, but to further proof its use, it would of course be instrumental to integrate it with the database of prepared shots for TCV and to apply it systematically pre-shot. The routine use of Fenix should naturally lead to the improvement of the accuracy of the reduced models inside it, and through that further increase the benefits of using this tool.

Acknowledgement

The authors want to thank Cassandre Contré and Simon Van Mulders for interesting and fruitful discussions about the reduced models used inside the RAPTOR code as well as the coupling between RAPTOR and the LIUQE and FBT equilibrium codes of the MEQ code suite. This work has been carried out within the framework of the EUROfusion Consortium, partially funded by the European Union via the Euratom Research and Training Programme (Grant Agreement No 101052200 — EUROfusion). The Swiss contribution to this work has been funded in part by the Swiss State Secretariat for Education, Research and Innovation (SERI). Views and opinions expressed are however those of the author(s) only and do not necessarily reflect those of the European Union, the European Commission or SERI. Neither the European Union nor the European Commission nor SERI can be held responsible for them. This work has in particular been supported by the EUROfusion Theory, Simulation, Verification and Validation (TSVV) projects TSVV11 and TSVV15.

Data availability statement

The data that support the findings of this study are openly available at the following URL/DOI: https://doi.org/10.5281/zenodo.19452938

Appendix A. Geometric profiles

Table 3 showed the quantities being exchanged between FGE and ASTRA. Some of the geometric profiles needed by ASTRA are not directly available in FGE output though. In particular, the values for the geometric profiles needed at the magnetic axis and at the diverted separatrix present some difficulties. To address this, approximations for the asymptotic values for the geometric profiles needed by ASTRA at the magnetic axis and at the diverted separatrix are derived in this appendix based on quantities available from FGE.

We start by listing some definitions and commonly known identities that will be used later on:

$$\langle f \rangle = \frac{\oint f/B_\theta dl_\theta}{\oint 1/B_\theta dl_\theta}, \tag{A.1}$$

$$\rho = \sqrt{\frac{\phi}{\pi B_0}}, \tag{A.2}$$

$$q = \frac{\partial \phi}{\partial \psi} = \frac{1}{2\pi} \oint \frac{B_\phi}{R B_\theta} dl_\theta, \tag{A.3}$$

$$\frac{\partial \rho}{\partial \psi} = \frac{q}{2\sqrt{\pi B_0 \phi}} = \frac{q}{2\pi B_0 \rho}, \tag{A.4}$$

$$|B_\theta| = \frac{|\nabla \psi|}{2\pi R}, \tag{A.5}$$

$$\partial V/\partial \psi = \oint dl_\theta / B_\theta. \tag{A.6}$$

In these equations, $\langle f \rangle$ is the flux surface average for a generic quantity f, ρ is the toroidal flux radius, q is the safety factor, B_θ is the poloidal magnetic field, θ is the poloidal angle, dl_θ is a line element along the flux surface in the poloidal plane such that $l_\theta = \oint dl_\theta$ is the length of the poloidal contour of the flux surface.

The majority of the geometric profiles that ASTRA needs require $\langle (\nabla \rho)^2 \rangle$, while from the FGE output, we have only quantities involving $\langle (\nabla \psi)^2 \rangle$ available. Using expression A.4 and realising this is a flux function, we get

$$\langle (\nabla \rho)^2 \rangle = \left\langle \left(\frac{\partial \rho}{\partial \psi} \right)^2 (\nabla \psi)^2 \right\rangle = \frac{q^2}{4\pi B_0 \phi} \langle (\nabla \psi)^2 \rangle. \tag{A.7}$$

The problem with this expression is that at the axis, both ϕ and $\nabla \psi$ go to zero, meaning this expression becomes undefined. On a diverted separatrix, this expression becomes likewise undefined since $\nabla \psi$ goes to zero, while q goes to infinity. As such, we need some limit values to extract $\langle (\nabla \rho)^2 \rangle$ from the output available from FGE. Similar derivations can trivially be made to get $\langle (\frac{\nabla \rho}{R})^2 \rangle$ from $\langle (\frac{\nabla \psi}{R})^2 \rangle$ etc.

Appendix A.1. Limit values on axis

In the limit of $\rho \to 0$, the shape of the flux surfaces close to the axis becomes perfectly ellipsoid. This

Accepted Manuscript

allows the poloidal flux to be written as

$$\psi \approx \psi_m + \frac{x^T H x}{2}, \nabla\psi \approx Hx, \tag{A.8}$$

where ψ_m is the poloidal flux at the axis and H is the Hessian of ψ at the axis

$$H = [\frac{\partial^2\psi}{\partial R^2}, \frac{\partial^2\psi}{\partial R\partial Z}; \frac{\partial^2\psi}{\partial R\partial Z}, \frac{\partial^2\psi}{\partial Z^2}]. \tag{A.9}$$

Both ψ_m and H are available in the FGE output. For simplicity we will assume $\psi_m = 0$ in the following derivations. We define a vector $x = (x_1, x_2)$ in the (R, Z) plane that points from the magnetic axis to a point in the plasma and express it in an axis system aligned with the two major axis of the ellipsoid (which can be found from H). This way, we find

$$2\psi = \lambda_1 x_1^2 + \lambda_2 x_2^2 \tag{A.10}$$

where λ_1 and λ_2 are the eigenvalues associated with each of the axis. The ellipsoidal flux surfaces can be parameterised as

$$x_1 = \sqrt{\frac{2\psi}{\lambda_1}} cos\theta, \quad x_2 = \sqrt{\frac{2\psi}{\lambda_2}} sin\theta \tag{A.11}$$

This way, we find

$$(\nabla\psi)^2 = \lambda_1^2 x_1^2 + \lambda_2^2 x_2^2 = 2\psi(\lambda_1 cos^2\theta + \lambda_2 sin^2\theta)$$
$$\approx \psi(\lambda_1 + \lambda_2) = \psi tr(H), \tag{A.12}$$

where $tr(H)$ is the trace of the Hessian H. In the last step, we assumed the $\lambda_1 \approx \lambda_2$ such that $\langle(\nabla\psi)^2\rangle \approx \psi tr(H)$ without the need to calculate the integrals in equation A.1 over this ellipsoid to obtain the flux surface average.

Next, the toroidal flux included inside the ellipsoid flux surface close to the axis can be approximated as

$$\phi \approx B_{\phi,m} A_\phi = \frac{2\pi\psi B_{\phi,m}}{\sqrt{\lambda_1\lambda_2}} = \frac{2\pi\psi B_{\phi,m}}{\sqrt{det(H)}} \tag{A.13}$$

where $B_{\phi,m}$ is the toroidal field on the magnetic axis, A_ϕ is the surface area of the considered flux surface, and $det(H)$ the determinant of H. Combining expressions A.12 and A.13, we can write

$$\frac{\langle(\nabla\psi)^2\rangle}{\phi} \approx \frac{\sqrt{det(H)}tr(H)}{2\pi B_{\phi,m}}. \tag{A.14}$$

Filling this out in expression A.7, we obtain

$$\langle(\nabla\rho)^2\rangle_m \approx \frac{q_m^2\sqrt{det(H)}tr(H)}{8\pi^2 B_0 B_{\phi,m}} \tag{A.15}$$

at the magnetic axis. Using the identity [13]

$$q_m = \frac{2\pi sign(I_p) T_m}{\sqrt{det(H)} R_m}, \tag{A.16}$$

with q_m, R_m, T_m the values of the safety factor, the major radius, and the current flux function at the magnetic axis, expression A.15 can be rewritten as

$$\langle(\nabla\rho)^2\rangle_m \approx \frac{sign(I_p) q_m tr(H)}{4\pi B_0}. \tag{A.17}$$

Hence, $\langle(\nabla\rho)^2\rangle$ is found to take a finite value on the magnetic axis. It should be remarked that the exact value of this quantity is not of great practical importance, since inside ASTRA it is only used in products with $\frac{\partial V}{\partial\rho}$ (see equations 1-3), which is exactly zero at the magnetic axis.

Appendix A.2. Limit values on diverted separatrix

A general flux surface average can be written as in A.1. Since $B_\theta = 0$ at the X-point, the flux surface average on the separatrix will be equal to the value of the integrant at the X-point (at least for nonzero, finite-valued integrands). This property can be exploited to reduce equation A.7 at the separatrix to

$$\langle(\nabla\rho)^2\rangle_{LCFS} = (\nabla\rho)_X^2 = \frac{(q\nabla\psi)_X^2}{4\pi B_0 \phi_b}, \tag{A.18}$$

where ϕ_b is the toroidal magnetic flux enclosed by the separatrix. To obtain an approximation for $q\nabla\psi$ at the X-point, we make use of the cylindrical approximation of the safety factor:

$$q_{cyl} = \frac{l_\theta}{2\pi R}\frac{B_\phi}{B_\theta}. \tag{A.19}$$

Note that compared to the conventional form of this, we have replaced the minor radius by $l_\theta/(2\pi)$. Combining this definition with expression A.5 yields $q\nabla\psi \approx l_\theta B_\phi$. Note that this step is not rigorous, it is an approximation to use the cylindrical safety factor here. Filling out this approximation in equation A.18, we finally obtain

$$\langle(\nabla\rho)^2\rangle_{LCFS} \approx \frac{l_{LCFS}^2 B_{\phi,X}^2}{4\pi B_0 \phi_b}. \tag{A.20}$$

Another quantity that needs evaluation at the seperatrix is $\partial V/\partial\rho$. For this we start from $\partial V/\partial\psi$ that is available from FGE.

$$\left(\frac{\partial V}{\partial\rho}\right)^{-1} = \frac{\partial\rho}{\partial\psi}\left(\frac{\partial V}{\partial\psi}\right)^{-1} = \frac{q}{2\pi B_0\rho}\left(\frac{\partial V}{\partial\psi}\right)^{-1}$$
$$= \frac{1}{4\pi^2 B_0\rho}\frac{\oint(B_\phi/R)dl_\theta/B_\theta}{\oint dl_\theta/B_\theta} = \frac{1}{4\pi^2 B_0\rho}\left\langle\frac{B_\phi}{R}\right\rangle \tag{A.21}$$

The third expression, obtained using equation A.4, is again undefined at a diverted separatrix since both q and $\frac{\partial V}{\partial\psi}$ go to infinity there. To move on from this, identities A.3 and A.6 are used in the next step, while in the last step the definition of the flux surface average A.1 is used. Thus, at the separatrix, we find

$$\left(\frac{\partial V}{\partial\rho}\right)_{LCFS} = 4\pi^2 B_0\rho_b\left\langle\frac{B_\phi}{R}\right\rangle_{LCFS}^{-1}$$
$$= 4\pi^2 B_0\rho_b\left\langle\frac{B_\phi}{R}\right\rangle_X^{-1} = \frac{4\pi^2 B_0\rho_b R_X}{B_{\phi,X}} \tag{A.22}$$

Accepted Manuscript

References

[1] Fable E, Janky F, Treutterer W, Englberger M, Schramm R, Muraca M, Angioni C, Kudlacek O, Poli E and Reich M 2022 *Plasma Phys. Controlled Fusion* **64** 044002

[2] Wu C, David P, Fable E, Frattolillo D, Grazia L D, Mattei M, Siccinio M, Treutterer W and Zohm H 2023 *Fusion Sci. Technol.* **80** 766–771

[3] David P, E Fable C W, Gehring M, Sieben M, Sieglin B, Tardini G and Treutterer W 2025 *Open plasma sci.* **1**

[4] Faugeras B 2020 *Fusion Eng. Des.* **160** 112020

[5] Nouailletas R, Gros G, Faugeras B, Artaud J F and Moreau P 2025 *Fusion Eng. Des.* **219** 115299

[6] Artaud J, Imbeaux F, Garcia J, Giruzzi G, Aniel T, Basiuk V, Bécoulet A, Bourdelle C, Buravand Y, Decker J, Dumont R, Eriksson L, Garbet X, Guirlet R, Hoang G, Huynh P, Joffrin E, Litaudon X, Maget P, Moreau D, Nouailletas R, Pégourié B, Peysson Y, Schneider M and Urban J 2018 *Nucl. Fusion* **58** 105001

[7] Faugeras B, Boulbe C, Frattollilo D, Giruzzi G, Falchetto G, Artaud J, di Grazia L, Mattei M, Iafrati M, Schneider M, Bin W and Mele A 2025 Pulse design simulator for jt-60sa *30th IAEA Fusion Energy Conference (IAEA FEC 2025)*

[8] Meneghini O, Slendebroek T, Lyons B, McLaughlin K, McClenaghan J, Stagner L, Harvey J, Neiser T, Ghiozzi A, Dose G, Guterl J, Zalzali A, Cote T, Shi N, Weisberg D, Smith S, Grierson B and Candy J 2024 *arXiv* **[physics.plasm-ph]** (*Preprint* 2409.05894v1)

[9] Clark R, Nurgaliev M, Khairutdinov E, Subbotin G, Welander A and Orlov D 2025 *Fusion Eng. Des.* **211** 114765

[10] Khayrutdinov R and Lukash V 1993 *J. Comput. Phys.* **109** 193–201

[11] Wang Z, Schuster E, Rafiq T, Huang Y, Luo Z, Yuan Q and Barr J 2025 *Fusion Eng. Des.* **215** 114969

[12] Carpanese F 2021 *Development of free-boundary equilibrium and transport solvers for simulation and real-time interpretation of tokamak experiments* Ph.D. thesis École Polytechnique Fédérale de Lausanne (EPFL)

[13] Moret J, Duval B, Le H, Coda S, Felici F and Reimerdes H 2015 *Fusion Eng. Des.* **91** 1–15

[14] Carpanese F, Felici F, Galperti C, Merle A, Moret J, Sauter O and the TCV team 2020 *Nucl. Fusion* **60** 066020

[15] Van Mulders S, Felici F, McIntosh S, Carpanese F, Contré C, Coosemans R, Kudláček O, Pastore F, Pinches S, Reisner M and Sauter O 2025 *Nucl. Fusion* **65** 066006

[16] Contré C, Merle A, Sauter O, Van Mulders S, Coosemans R, Durr-Legoupil-Nicoud G, Felici F, Février O, Heiß C, Labit B, Pau A, Poels Y, Venturini C, Vincent B, the TCV team and the EUROfusion Tokamak Exploitation Team 2026 *Submitted to Nucl. Fusion* **[arXiv physics.plasm-ph]** (*Preprint* 2603.01210v2)

[17] Heiß C, Merle A, Carpanese F, Felici F, Donner C, Marchioni S, Mari A and Sauter O 2026 *Plasma Phys. Controlled Fusion* **in press**

[18] Mele A, Tenaglia A, Carnevale D, Coda S, Felici F, Galperti C, Merle A, Pironti A, Sauter O, the TCV team and the Eurofusion Tokamak Exploitation team 2024 Design of a novel plasma shape controller for the tcv tokamak *10th International Conference on Control, Decision and Information Technologies (CoDIT)* pp 284–289

[19] Ivanov A, RRKhayrutdinov, Medvedev S Y and Poshekhonov Y Y 2005 New adaptive grid plasma evolution code SPIDER *32nd EPS Conference on Plasma Phys.* vol 29C pp P–5.063

[20] Fable E, Tardini G, Giannone L and the ASDEX Upgrade Team 2025 *Open plasma sci.* **1**

[21] Pereverzev G and Yushmanov Y 2002 Benchmarking of the nbi block in the astra code versus the ofmc calculations IPP Report 5/98

[22] Tardini G *et al.* 2026 *submitted to PPCF*

[23] Van Mulders S, Sauter O, Bock A, Burckhart A, Contré C, Felici F, Fischer R, Schramm R, Stober J, Zohm H and the ASDEX Upgrade Team 2024 *Nucl. Fusion* **64** 026021

[24] Siccinio M, Fable E, Angioni C, Saarelma S, Scarabosio A and Zohm H 2018 *Nucl. Fusion* **58** 016032

[25] Muraca M, Fable E, Angioni C, Luda T, David P, Zohm H, Siena A D and the ASDEX Upgrade Team 2023 *Nucl. Fusion* **65** 035007

[26] Sauter O, Angioni C and Lin-Liu Y R 1999 *Phys. Plasmas* **6** 2834–2839 errata in ibidem 9 (2002) 5140

[27] A Polevoi H S and Takizuka T 1997 Astra automated system for transport analysis JAERI-Data/Code 97-014

[28] Geelen P, Felici F, Merle A and Sauter O 2015 *Plasma Phys. Controlled Fusion* **57** 125008

[29] Teplukhina A, Sauter O, Felici F, Merle A, Kim D, the TCV Team, the ASDEX Upgrade Team and the EUROfusion MST1 Team 2017 *Nucl. Fusion* **59** 124004

[30] Martin Y R, Takizuka T and the ITPA CDBM H-mode Threshold Database Working Group 2008 *J. Phys.: Conf. Ser.* **123** 012033

[31] Schmidtmayr M, Hughes J, Ryter F, Wolfrum E, Cao N, Creely A, Howard N, Hubbard A, Lin Y, Reinke M, Rice J, Tolman E, Wukitch S, Ma Y, the ASDEX Upgrade Team and Alcator C-Mod Team 2018 *Nucl. Fusion* **58** 056003

[32] Angioni C and Sauter O 2000 *Phys. Plasmas* **7** 1224–1234

[33] Hirshman S and Neilson G 1986 *Phys. Fluids* **29** 790–793

[34] Grad H and Rubin H 1958 *J. Nucl. Energy* **7** 284–285

[35] Shafranov V 1958 *Sov. Phys. JETP* **6** 545–554

[36] Lütjens H, Bondeson A and Sauter O 1996 *Comput. Phys. Commun.* **97** 219–260

[37] Galperti C, Felici F, Vu T, Sauter O, Carpanese F, Kong M, Marceca G, Merle A, Pau A, Perek A, Pesamosca F, Baquero-Ruiz M, Coda S, Decker J, Duval B, Gospodarczyk M, Karpushov A, Marchioni S, Maier A, Marletaz B, Segovia A, Vincent B, Yildiz C, Carnevale D, Ferron N, Koenders J, Kool B, Manduchi G, Maraschek M, Milne P, Neto A, Poli E, Ravensbergen T, Reich M, Rispoli N, Sartori F and the TCV team 2024 *Fusion Eng. Des.* **208** 114640

[38] Sauter O, Vallar M, Labit B, Karpushov A, Bagnato F, Coda S, Merle A, Pütterich T, Bobkov V, Dunne M, Lang P, Maraschek M, Mcdermott R, Neubert P, Stober J, Suttrop W, Willensdorfer M, Voitsekhovitch I, Camenen Y, Widmer F, Eriksson T, Fransson E, Mantsinen M, the TCV Team, the ASDEX-Upgrade Team and the EUROfusion MST1 Team 2021 Iter baseline scenario investigations on TCV and comparison with AUG *28th IAEA Int. Conf. on Fusion Energy* pp EX/P4–887

[39] Labit B, Sauter O, Pütterich T, Bagnato F, Camenen Y, Coda S, Contré C, Coosemans R, Eriksson F, Février O, Fransson E, Karpushov A, Krutkin O, Marchioni S, Merle A, Pau A, Piron L, Vallar M, Van Mulders S, Voitsekhovitch I, the TCV team, the MST1 team and the EUROfusion tokamak exploitation team 2024 *Plasma Phys. Controlled Fusion* **66** 025016

[40] Moret J M, Buhlmann F, Fasel D, Hofmann F and Tonetti G 1998 *Rev. Sci. Instrum.* **69** 2333–2348

[41] Coda S, Balestri A, Ball J, Porte L, Février O, Merle A, Sauter O and the TCV Team 2023 Optimization of shape for confinement in negative-triangularity diverted tokamak plasmas *49thEPS Conference on Plasma Physics* vol 47A pp Fr–MCF47

[42] Staebler G, Candy J, Howard N and Holland C 2016 *Phys. Plasmas* **23** 062518

[43] Angioni C, Gamot T, Tardini G, Fable E, Luda T, Bonanomi N, Kiefer C, Staebler G, the ASDEX

Accepted Manuscript

Upgrade Team and the EUROfusion MST1 Team 2022
Nucl. Fusion **62** 066015

Accepted Manuscript